Self-propelled motion switching in nematic liquid crystal droplets in aqueous surfactant solutions

Mariko Suga,[1] Saori Suda,[2] Masatoshi Ichikawa,[2] and Yasuyuki Kimura[1,*]
[1]*Department of Physics, School of Science, Kyushu University, 744 Motooka, Nishi-ku, Fukuoka 819-0395, Japan*
[2]*Department of Physics, Graduate School of Science, Kyoto University, Kitashirakawa-Oiwakecho, Sakyo-ku, Kyoto 606-8502, Japan*

(Received 18 March 2018; published 14 June 2018)

The self-propelled motions of micron-sized nematic liquid crystal droplets in an aqueous surfactant solution have been studied by tracking individual droplets over long time periods. Switching between self-propelled modes is observed as the droplet size decreases at a nearly constant dissolution rate: from random to helical and then straight motion. The velocity of the droplet decreases with its size for straight and helical motions but is independent of size for random motion. The switching between helical and straight motions is found to be governed by the self-propelled velocity, and is confirmed by experiments at various surfactant concentrations. The helical motion appears along with a shifting of a point defect from the self-propelled direction of the droplet. The critical velocity for this shift of the defect position is found to be related with the Ericksen number, which is defined by the ratio of the viscous and elastic stresses. In a thin cell whose thickness is smaller than that of the initial droplet size, the droplets show more complex trajectories, including "figure-8s" and zigzags. The appearance of those characteristic motions is attributed to autochemotaxis of the droplet.

DOI: 10.1103/PhysRevE.97.062703

I. INTRODUCTION

Active matter, objects with self-propelling mechanisms or similar properties, have recently attracted the interests of researchers [1–4]. Typical examples of microscopic active matter include microorganisms and plankton [3,4]. Corresponding artificial systems with self-propelling mechanisms have also been intensively studied from theoretical and experimental viewpoints [1,2,5,6]. These artificial objects are driven by a spatial gradient in a local field, such as temperature, concentration, or applied electric and magnetic field. For example, camphor beads floating at an air-water interface exhibit various types of characteristic motion due to the asymmetry of surface tension induced by the concentration gradient of the dissolved camphor [7–9]. Various chemical systems composed of oil droplets in aqueous surfactant solutions, or their inverse systems, have also been reported to exhibit self-propulsion. Most of these systems are driven by convective flow induced by the Marangoni stress due to the gradient of surface tension along their surfaces [10–23].

In addition to random motion, straight and circular trajectories have been reported experimentally for artificial active droplets [17,20]. Recently, helical motion by droplets composed of both nematic [24] and cholesteric liquid crystals [25] has also been reported experimentally, and predictions of helical motion have also been made for systems with deformable particles [5,26,27]. In self-propelled liquid crystal droplets, the appearance of a helical motion is thought to relate with the coupling between the molecular alignment and the convective flow induced by the Marangoni stress inside the droplet [24]. Because the alignment of a liquid crystal is determined by the competition between forces at the surface and those in the bulk, spatial confinement is expected to be an important factor for controlling their motion. The liquid crystal droplets in aqueous surfactant solution dissolve slowly, so we can change their size during the elapsed time.

In this study, we have experimentally studied the effect of the size of a nematic droplet on its motion by observing the dissolution process of individual droplets over long time periods. We have also studied the influence of the dimensionality of the system on the motion of the droplets by using a two-dimensionally confined cell.

II. EXPERIMENT

We dispersed a droplet of nematic liquid crystal, 4-pentyl-4′-cyanobiphenyl (5CB, TCI) in a 10 wt% aqueous solution of tetradecyl trimethyl ammonium bromide (TTAB, Sigma-Aldrich). Since the density of 5CB is slightly larger than that of the surfactant solution, an appropriate quantity of heavy water (UVasol, Merck) was added to the aqueous phase to match the density of the solvent with the droplet. We filled the surfactant solution inside a silicone rubber ring with an inner diameter of 1 cm and a thickness of 2 mm or 100 μm [Fig. 1(a)]. A nematic droplet was prepared by injecting the appropriate amount of 5CB into the surfactant solution using a microinjector (femtojets 4i, Eppendorf) [25]. By changing the injection pressure and time to jet, the size of the droplet can be varied over a range of 20–200 μm. After that, a cover slip was used to enclose the cell. Hereafter we refer to the cell with the 2 mm ring as the 3D system and the cell with the 100 μm ring as the 2D system. Only a few droplets of the same size were dispersed in a cell at one time to reduce the interactions between them.

The temperature was fixed at 25 °C in the nematic phase during the experiments. The dissolution rate of a droplet is rather small compared with that reported in previous studies

*kimura@phys.kyushu-u.ac.jp

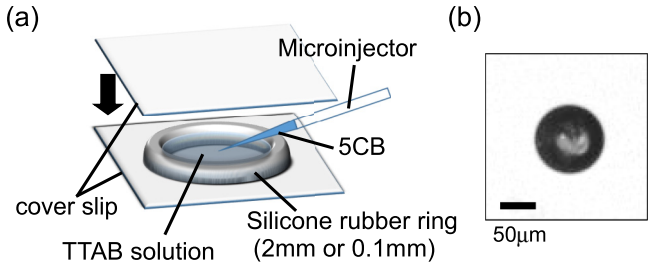

FIG. 1. Experimental setup: (a) Schematic of the preparation steps for the sample cell. A droplet of 5CB of the appropriate size is injected into a surfactant solution using a microinjector. The thickness of the cell is controlled using the silicone rubber ring. The solution is enclosed with a cover slip after the droplets are injected. (b) A bright-field microscope image of a nematic droplet dispersed in an aqueous mixture solution of TTAB and D_2O at 25 °C.

[24,28]. It took about 3 h for a droplet with an initial size of 120 μm to dissolve completely. Observations were started about 2 min after the injection of the droplet. The motion of a single 5CB droplet was observed using an inverted microscope (Eclipse Ti, Nikon) with a 4× objective lens (PlanFlour, NA = 0.13, Nikon). The obtained microscope images were captured with a CCD camera (ADT-100, Flovel, 1000 × 1000 pixel^2, 10 bits) at 30 frames/s. In larger droplets, large fluctuations in the orientation of the liquid crystal were observed, as shown in Fig. 1(b). We observed the motion of each droplet for 30–60 s at the time intervals of 1 to 10 min. The trajectories of the droplets and their sizes were analyzed using ImageJ.

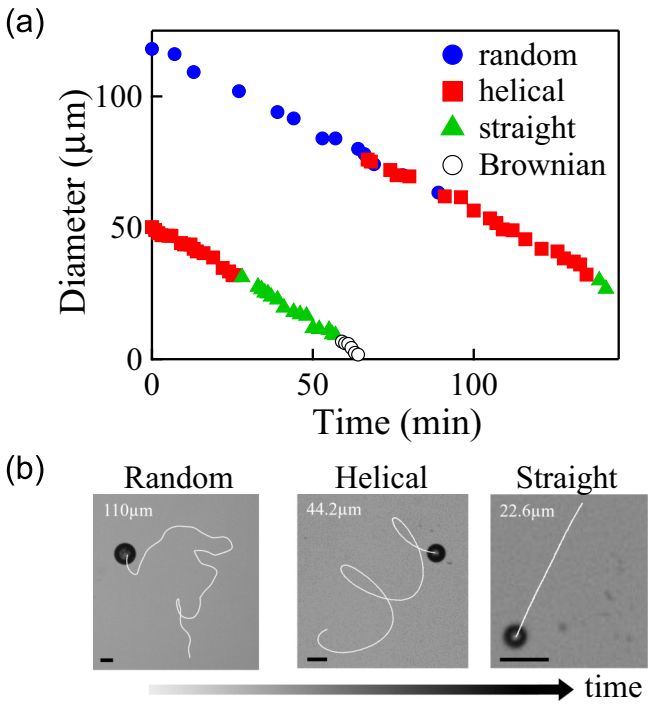

FIG. 2. Change in self-propelled motion of a nematic liquid crystal droplet in the 3D system. (a) Change in diameter over time for two droplets with different initial sizes. Different symbols represent different modes of motion. (b) Characteristic trajectories of a droplet over 30 s. By decreasing the droplet size or waiting for time to elapse, the motion was observed to change random → helical → straight. The scale bars represent 50 μm.

III. SELF-PROPELLED MOTION OF A NEMATIC DROPLET IN THE 3D SYSTEM

A. Switching of self-propelled motion with droplet size

The self-propelled mechanism of a nematic droplet in a surfactant solution has been investigated by Herminighaus *et al*. [23] The self-propulsion is induced by the Marangoni flow originated by the symmetry breaking in the adsorption of the surfactant molecules to the droplet. The propulsion maintains by the dissolution of nematic molecules, which results in the depletion of empty micelles at the rear side of the droplet, and this keeps the gradient of the surfactant molecules along the droplet.

Figure 2(a) shows the temporal change in the diameter of two nematic droplets with different initial sizes. The solubilization rate of the droplet diameter is nearly constant for both droplets. A linear decrease over time in the droplet size has been reported for both nematic [28] and isotropic droplets [29]. The linear dependence holds when the solubilization zone is much thinner than the droplet size [29]. As a result, deviations from linearity are seen with the smaller droplets.

We also find that the droplet changes its characteristic motion with decreasing the size as random → helical → straight one. Typical trajectories of respective motions are shown in Fig. 2(b). A droplet whose diameter is smaller than about 10 μm exhibits Brownian-like random motion. The critical sizes between the self-propelled motion modes are similar for two droplets with different initial sizes, as shown in Fig. 2(a). This indicates that motion mode switching is controlled by the size of the droplets.

The crossovers from random to helical motion, and from helical to straight motion, are found to occur at droplet diameters of about 60 and 30 μm, respectively. This kind of switching in the self-propelled motion already has been reported for isotropic droplets suspended at an air-water interface, both experimentally and theoretically [17,20]. In addition, a phenomenological theory of self-propelled objects in three dimensions, which accounts for the coupling between self-propelled motion, the deformation of a droplet, and the rotational motion, predicts the appearance of straight, circular and spiral motions [26,27]. According to these theories, straight motion becomes unstable at larger velocities, so circular and helical (spiral) motion spontaneously appear.

The characteristic temporal evolution of the mean square displacement (MSD) for the two-dimensional (2D) trajectories of random, helical, straight, and Brownian-like motions are shown in Fig. 3(a). For random motion, the MSD is approximately proportional to t^2 over short time periods, but scaled at t over long time intervals, due to the frequent changes of direction. However, the MSD for helical and straight motion is proportional to t^2, at both short and long timescales. For helical motion, the former value corresponds to motion along a circular path over short time, and the latter relates to the straight motion of a droplet along the axis of a helical trajectory. For Brownian-like motion, the MSD is approximately proportional

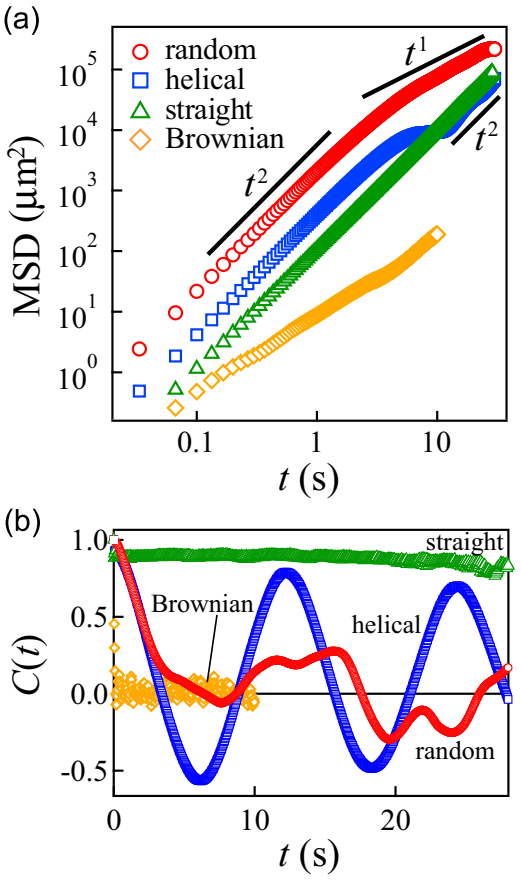

FIG. 3. Mean square displacement (MSD) and angular autocorrelation function $C(t)$ for random, helical, straight, and Brownian-like motions. (a) MSD calculated from a single droplet trajectory. (b) $C(t)$ calculated from the instantaneous velocities.

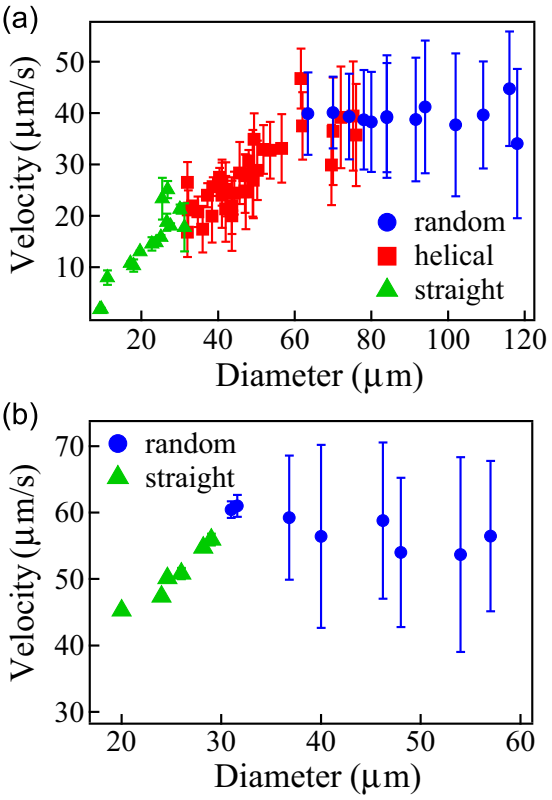

FIG. 4. Dependence of the averaged instantaneous 2D projected velocity on the diameter of the droplet in 10 wt% TTAB solution. Different symbols represent different modes of the self-propelled motion. (a) Nematic phase at 25 °C. (b) Isotropic phase at 40 °C.

to t but seems to be slightly superdiffusive. We can distinguish those motions based on the temporal dependence of the MSD.

The characteristics of respective motions are also distinguished by the angular autocorrelation function $C(t)$ of the instantaneous 2D velocities $\boldsymbol{v}(t)$ defined by $C(t) = \langle \frac{\boldsymbol{v}(t+t_0)\cdot\boldsymbol{v}(t_0)}{|\boldsymbol{v}(t+t_0)||\boldsymbol{v}(t_0)|} \rangle_{t_0}$, where $\langle \cdots \rangle_{t_0}$ denotes the time average over t_0. The temporal evolution of $C(t)$ for random, helical, straight, and Brownian-like motions are shown in Fig. 3(b). For random and Brownian-like motions, the correlation decays exponentially with time due to the change of the direction in their translational motion. The correlation time is much larger in the random motion, and there is oscillatory component which is remnant of the helical motion. For helical motion, the correlation shows the oscillation behavior with slightly decaying amplitude. However, the decaying time is similar to that observed in the straight motion. This indicates the axis of helical motion is almost a straight one. We regard the period oscillation observed in $C(t)$ as the period of helical motion.

The dependence of the 2D projected instantaneous velocity averaged over 1 s on the diameter of the droplet is shown in Fig. 4(a). The velocity shows a linear dependence on the droplet diameter in regions of straight or helical motion. However, the velocity is independent of the droplet size in regions with random motion. From the captured images, larger droplets tend to approach the cell wall, which is partially due to imperfect density matching. An isotropic water droplet in oil exhibits both straight and circular motions near the wall. Its self-propelled velocity is found to be independent of the type of motion [30], which is consistent with nematic droplets undergoing random motion.

In the stationary state, the driving force of self-propulsion F is balanced with the viscous force ζv, where ζ is the friction coefficient and v is the self-propelled velocity. ζ is proportional to ηR for a spherical droplet [31], where η is the effective viscosity of the medium and R is the radius of the droplet. When we assume that F is proportional to the surface area of the droplet R^2, v will be proportional to R.

However, when the droplet is near the cell wall, the viscous dissipation is mainly due to the flow at the gap Δ between the wall and the droplet. The viscous energy dissipation per unit time can be estimated by $\eta(v/\Delta)^2\pi R^2\Delta/2$. In the stationary state, this dissipation is balanced by the work done by the driving force per unit time, based on the value of Fv. This suggests that v is independent of R.

In Fig. 4(b) the self-propelled motion of a 5CB droplet in the isotropic phase at 40 °C is shown for comparison. The droplet also dissolves with an almost constant solubilization rate for the size, but the rate is much larger than at 25 °C. Similar to nematic droplets, larger droplets exhibit random motion, and smaller ones show straight motion. The helical motion disappears in the

isotropic phase, which agrees with a previous report [24]. This confirms that the appearance of helical motion is characteristic of nematic droplets. The critical diameter between random and straight motion is about 30 μm. This is on the same order as the transition value between helical and random motion in the nematic phase. In the region of straight motion, the velocity increases with droplet size, while for random motion, the velocity tends to saturate at about 55 μm/s. This is larger than the corresponding value in the nematic phase, as seen in Fig. 4(a).

B. Characteristics of helical motion

The temporal changes in the characteristics of the helical trajectories, the rotational period T, the helical pitch p, and the radius of the helix r are evaluated. The period T is determined from the temporal oscillations in the angular autocorrelation function $C(t)$ [see Fig. 3(b)]. The dependence of T on the diameter of the droplet is shown in Fig. 5(a). The value of T does not show any apparent size dependence over 10–20 s. The apparent pitch p is plotted against the diameter of the droplet in Fig. 5(b). Although p depends on the tilt of the helical axis from the observation plane, the droplets are found to show little vertical displacement during observation. p shows no apparent size dependence over the range of about 100–150 μm. The dependence of the radius r on the velocity of the droplet is shown in Fig. 5(c). There are large errors in the experimental data, but r tends to decrease with decreasing droplet velocity. From the best-fit line of the data, the helical path disappears ($r \to 0$) at about 19.4 μm/s.

Since the velocity along the helical axis v_p can be estimated using p/T, v_p is almost constant over the range of helical motion. Conversely, since the tangential velocity v_t can be estimated using $2\pi r/T$, v_t increases with the droplet size. The average velocity $\bar{v}_h$ for helical motion is estimated using the time average of $\sqrt{v_p^2 + v_t^2}$ over T as $\bar{v}_h = 2v_t \mathrm{E}(\frac{\pi}{2},k)/\pi k$, where $k = v_t/\sqrt{v_p^2 + v_t^2}$ and $\mathrm{E}(\frac{\pi}{2},k)$ is the complete elliptic integral of the second kind. Since the contribution of v_t is dominant, the value of $\bar{v}_h$ increases linearly with the droplet size over the range of helical motion [Fig. 4(a)].

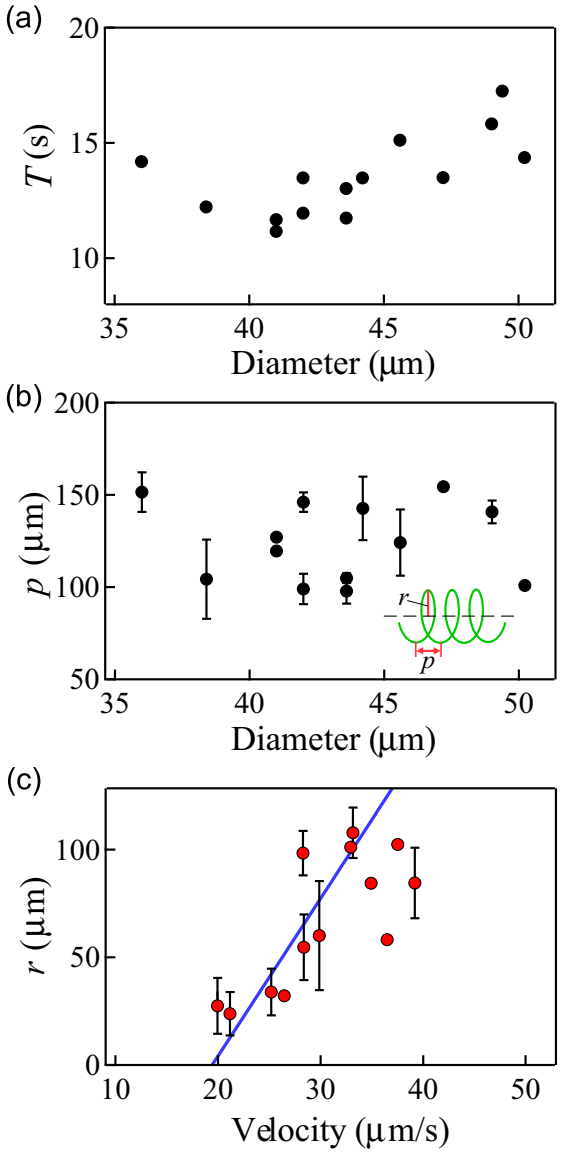

FIG. 5. Characteristic parameters of helical motion: (a) Dependence of rotational period T on the diameter of the droplet. (b) Dependence of the pitch p of the helical trajectory on the diameter of the droplet. (c) Dependence of radius r of the helical trajectory on the velocity of the droplet. The extrapolated best-fit line to the data crosses the zero-radius axis at 19.4 μm/s. The definitions of p and r are shown in the inset of (b).

C. Dependence of switching between self-propelled motion modes on the concentration of surfactant solution

To determine the primary factors that induce the observed switching between the self-propelled motions, we change the driving force by varying the concentration of the surfactant solution. It has been reported that the velocity of a droplet increases monotonously with the concentration of TTAB up to 20 wt% [22,23]. We have also studied the self-propelled motion in solutions containing 3.75 or 7.5 wt%. In Fig. 6 the self-propelled velocity is plotted against the diameter of the droplets for all TTAB concentrations. Although the overall trends are similar, the critical values between the observed modes appear different.

The boundary between random and helical motion appears to be around a diameter value of 70 μm. However, the velocity during random motion increases along with the concentration of TTAB. Since the switching of the modes is affected by interactions with a wall, as discussed before, it is expected to depend strongly on the droplet size. However, the crossover between helical and straight motion is found to be determined primarily by the velocity, with a switch occurring around 20–25 μm/s. The critical size for this transition increases with decreasing TTAB concentration. This is consistent with the previous result for switching between straight and circular motions in an isotropic oil droplet [17,20]. The relationships of the critical size and the critical velocity for switching between self-propelled modes are summarized in Table I.

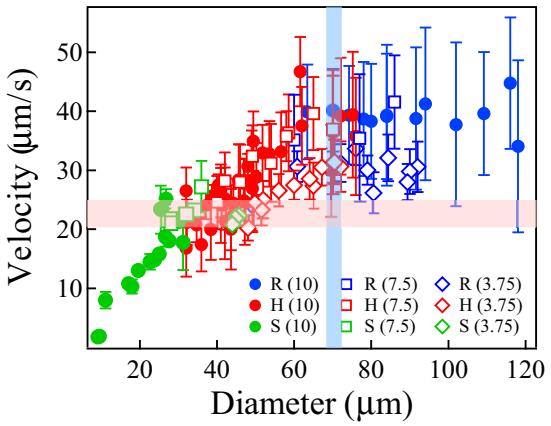

FIG. 6. Dependence of the self-propelled velocity on the diameter of droplet for various TTAB concentrations: 3.75, 7.5, and 10 wt%. For all concentrations, the droplets show random (R), helical (H), or straight (S) motion as their sizes decreased. The boundary between the R and H motion appears to be governed by size, which is marked with a thick vertical line. The crossover between H and S motion was governed by velocity, as marked with a thick horizontal line.

D. Motion of a point defect during helical motion

Since the 5CB molecules align themselves normal to the droplet surface, a point defect at the center of the droplet spontaneously appears. Herminghaus *et al*. [23] reported that this defects moves toward the stagnation point of convective flow when the droplet is placed in a constant flow of a surfactant solution. Krüger *et al*. [24] reported that the helical motion of nematic droplets is due to symmetry breaking at the location of a defect. Once a point defect shifts its position due to fluctuations from the stagnation point during convection, the defect stays at the position where the viscous force balances the elastic distortion force. The polar position of the defect is expected to increase monotonously with the velocity of convection. Due to the isotropic orientation of the liquid crystal at the core of the defect, the viscosity decreases, while the velocity of convection increases near the defect. The gradient in the convection velocity induces torque on the droplet, and it starts to rotate. Therefore, the circular motion originates from a shift of a point defect away from its propelling direction. In addition, an autochemotactic force that prevents the droplet from crossing its previous trajectory transforms the circular motion into helical one.

TABLE I. Relationships between the critical size and critical velocity thresholds for switching between straight (S) to helical (H), or helical (H) to random (R) motion, and Ericksen number (E_r) at the S-H transition, on the concentration of TTAB.

TTAB concentration (wt%)	10	7.5	3.75
S-H critical size (μm)	31.6 ± 0.4	38 ± 2	46.8 ± 1.2
S-H critical velocity (μm/s)	21 ± 7	24 ± 4	20 ± 2
H-R critical size (μm)	70 ± 6	68 ± 9	66 ± 6
H-R critical velocity (μm/s)	38 ± 2	36 ± 1	28 ± 3
E_r (S-H)	1.4 ± 0.5	2.0 ± 0.4	2.0 ± 0.3

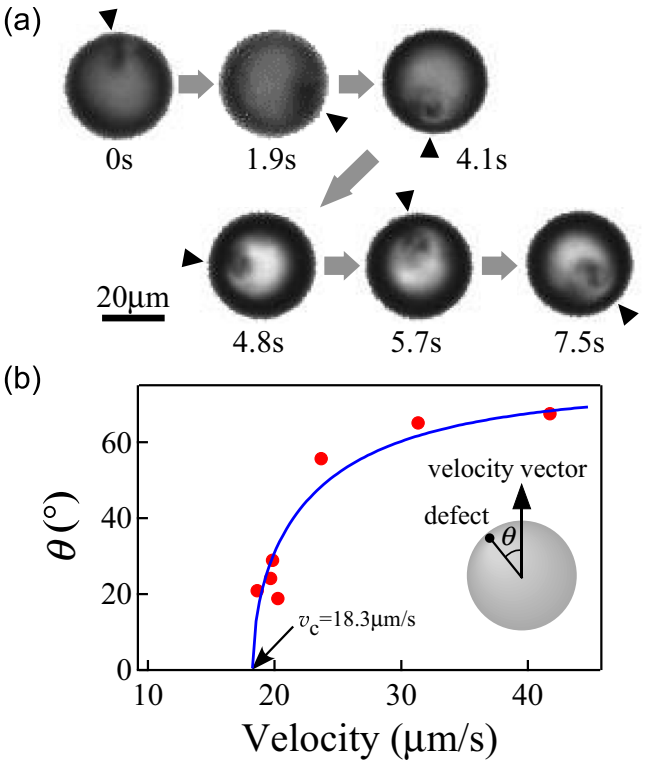

FIG. 7. The motion of a defect during helical motion. (a) Time series of bright-field microscope images. The contrast was controlled to make the defect more easily identifiable. The black point indicated by a triangle is a point defect. (b) The dependence of the polar angle θ on the velocity of a droplet. The solid line represents the best-fit approximate curve obtained by dimensional analysis. The schematic shows the definition of polar angle θ. v_c =18.3 μm/s is the critical velocity for which the defect begins to shift its position away from the velocity vector.

We directly observe changes of the polar position of a defect θ in a self-propelled droplet under higher magnification (15×). Figure 7(a) shows the time series of microscope images of a droplet, whose propelling direction was perpendicular to the plane of observation (from back to front). The defect noticeably shifts its position from the center of the droplet. We also find that its azimuthal position rotates around its propelling velocity vector with a period of 6–8 s. This rotational period does not have any apparent dependence on the velocity. Figure 7(b) shows the dependence of θ on the average velocity of the droplet. θ suddenly appears around 20 μm/s and saturates at about 70° for large velocities.

The position of a defect θ is determined by the balance between the viscous force and the elastic force. An exact calculation of the deformation of the molecular alignment and flow field over the whole droplet is difficult. Here we consider only the local deformation of alignment in liquid crystals for small values of θ. We estimated both contributions using dimensional analysis. The local viscous stress around the defect was estimated to be $v\eta \sin\theta/R$, where η is the effective viscosity of liquid crystal at the defect, v is the velocity of convective flow, and R is the radius of a droplet. The local elastic stress was estimated to be $k\theta/R^2$, where k is the elastic constant of liquid crystal. Based on the balance of these two

stresses for small θ, $v\eta\theta(1-\theta^2/6)/R \sim k\theta/R^2$, the solution of $\theta \neq 0$ is $\theta \sim \sqrt{1-k/(v\eta R)}$. Since we found $v \propto R$ in our experiment, R can be written as $R = v/\alpha$, where α is a positive constant. Therefore, the dependence of θ on v can be written as $\theta \sim \sqrt{1-v_c^2/v^2}$. The critical velocity v_c for the appearance of the solution of $\theta \neq 0$ is given by $v_c \equiv \sqrt{k\alpha/\eta}$.

The experimentally obtained dependence of θ on v in Fig. 7(b) is fitted by $\sqrt{1-v_c^2/v^2}$ as shown the solid line. The obtained $v_c = 18.3$ μm/s is consistent with a value of 19.4 μm/s, as estimated from Fig. 5(c). The experimental value of v_c is also close to the estimated value of $\sqrt{k\alpha/\eta} = 16.8$ μm/s from the reported values of η and k for 5CB at room temperature [32]: $k = k_3 = 8.2 \times 10^{-12}$ N, $\eta = 35$ mPa·s, and the measured value of $\alpha = 1.20$ s^{-1} from Fig. 4(a). We used the value of $\eta = \eta_2/3$ as the viscosity of the defect core, as noted by Krüger *et al*. [24]

The onset of helical motion is controlled by the parameter of $v\eta R/k$. This dimensionless parameter is known as the Ericksen number, E_r, and gives the ratio of viscous to elastic forces [32]. The critical values of E_r for switching to helical motion for various TTAB concentrations are of the order of unity and are listed in the last column of Table I. The observed critical E_r values exhibit slight dependence on TTAB concentration, which is different from that predicted by our rough estimation. Yamamoto reported the E_r value for the onset of helical motion in cholesteric liquid crystals to be $E_r \approx 3$ [25]. The definition of E_r used by Yamamoto is about twice that used in this paper. Therefore, the critical value of E_r observed in this study appears to be consistent with the finding of the cholesteric system. A more complete theoretical discussion based on nemato-hydrodynamics is necessary to understand the switching between straight and helical motion.

The origin of the spinning motion of a droplet about its self-propelled velocity vector is not clear at this point. The observed spinning motion will modulate the circular motion, which results in helical motion about the circular trajectory. Such flowerlike or superhelical trajectories have been reported both in experiment [24] and in simulations of deformed particle systems [27].

IV. SELF-PROPELLED MOTION IN THE 2D SYSTEM

The motion of a droplet in a spatially confined system is observed by using a 100-μm-thick cell. Its thickness was chosen to be smaller than the initial diameter of an droplet. The various characteristic motions differ from those observed in the 3D system, as shown in Fig. 8(a). By decreasing in the size of the droplet, the trajectory changes from a "figure-8," to random, zigzag, or straight.

The temporal change of droplet size is shown in Fig. 8(b). The dependence has an inflection point around 100 μm, which corresponds with the thickness of the cell. We also plot the diameter of the equivalent spheres, whose volumes are equal to those of the pancake-shaped droplets. The dependence has a similar slope to that seen for the 3D regime.

In the regime for which the droplet exhibits a "figure-8" or random motion, the droplet is sandwiched between the walls and is significantly deformed from its spherical shape. This situation can be regarded as a quasi-2D system. Since friction from the walls becomes larger, the velocity is expected

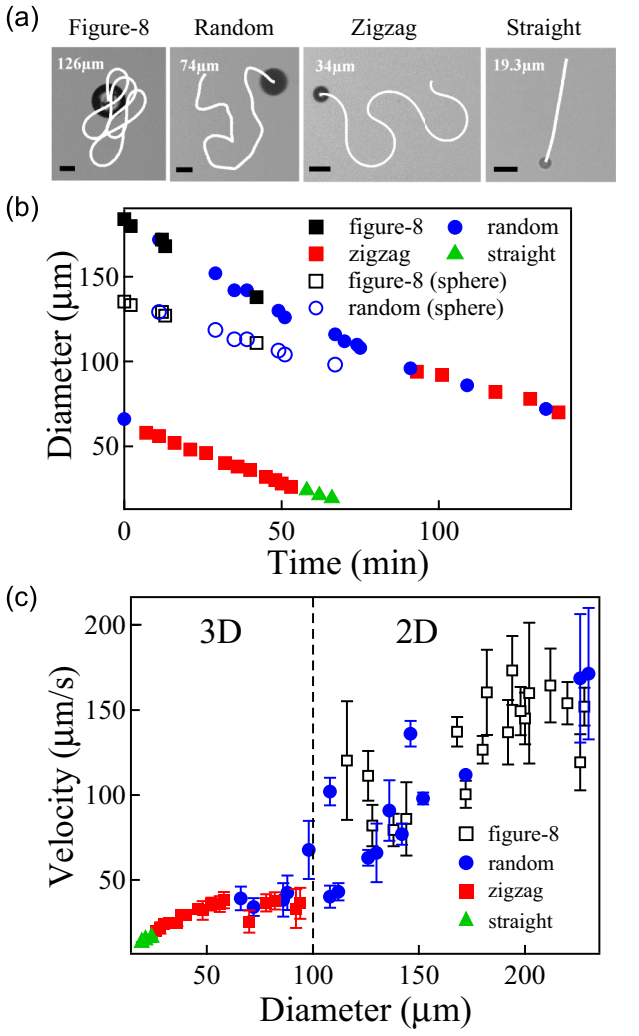

FIG. 8. Characteristic motions of a self-propelled 5CB droplet in the 2D system. The concentration of the TTAB aqueous solution is 10 wt%. (a) Typical trajectories of droplets of various sizes: "figure-8", random, zigzag, and straight. The scale bars represent 50 μm. (b) Temporal change of droplet diameter. The data marked with empty symbols represent the diameters of spheres with equivalent volumes. (c) Dependence of the averaged instantaneous 2D projected velocities on the diameter of the droplets. Different symbols represent different types of motion.

to decrease with increases in the size. However, the velocity increases with size, similar to the effect seen in the 3D system, as shown in Fig. 8(c). This is partially due to a negative autochemotactic effect [24,33], which is a "negative phoretic" behavior in that the droplet tends to avoid areas where it previously passed. In a thin cell, the diffusion of the liquid crystal in solution become slower and its concentration increases at the trailing side of the droplet. This gradient pushes the droplet to more dilute regions and is expected to significantly accelerate the self-propelled motion.

When the size of droplet is smaller than that of the cell thickness, the dependence resembles that seen in the 3D case [Fig. 4(a)]. The region in which the zigzag motion is observed corresponds to that of helical motion in the 3D system. Therefore, the zigzag motion can be regarded as a

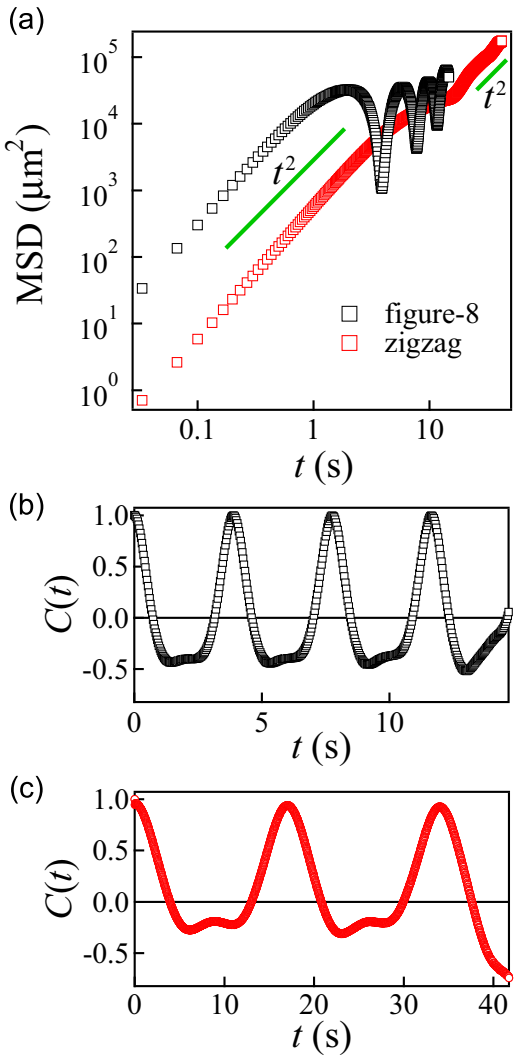

FIG. 9. Temporal change of MSD and $C(t)$ for figure-8 and zigzag motions. (a) MSD for figure-8 and zigzag motions. (b) $C(t)$ for figure-8 motion. (c) $C(t)$ for zigzag motion.

modified helical motion. Because the cell thickness is smaller than in the 3D system, the motion of the droplet becomes slower, and the concentration of liquid crystals near the droplet slowly relaxes. The droplet avoids crossing its past trajectories, and the helical motion is transformed into a zigzag mode in thin cells.

The temporal change of MSD and the angular correlation function $C(t)$ for figure-8 and zigzag motions are shown in Figs. 9(a)–9(c). The MSD for figure-8 motion is approximately proportional to t^2 over short time periods but oscillates with time over long time intervals. $C(t)$ also shows oscillatory behavior, and the oscillation is asymmetric about zero. The MSD for zigzag motion looks like that of helical motion, but $C(t)$ rather looks like that of figure-8. Between these two modes, the random motion appears and is characterized by the oscillatory decaying function of $C(t)$, which similar to that in Fig. 3(b).

V. CONCLUSION

The self-propelled motion of a nematic liquid crystalline droplet in an aqueous surfactant solution has been studied by tracking single droplets over long time periods. The characteristic motion switches depending on the droplet size and self-propelled velocity. The switch between straight and helical motion modes is found to be controlled by the velocity. At the critical velocity, the straight motion becomes unstable and a defect shifts away from the self-propelled direction. This induces a tangential velocity gradient and changes the direction. A spinning mode for the droplets is also observed. The origin of this spinning motion is still not well understood.

The switching of self-propelled modes with velocity is theoretically studied using a phenomenological model, in which the translational velocity, the deformation of a particle, the spinning motion, and their interactions are taken into account [5,26,27]. In three dimensions, the straight, circular, and helical modes have been observed with increasing velocity of the droplet. Although the nematic droplet barely deforms from its spherical shape, the deformation of the director field in nematic droplets can be expressed in a tensor form similar to the particle deformation. Therefore, it is expected that tuning the parameters in the theory will help to understand what is observed in this study using a phenomenological model [26,27,34]. However, in a nematic droplet, the circular motions have not been observed as a transition between the straight and helical motions.

Even under strongly confined condition, the droplet can propel itself to a large velocity. One origin of this characteristic motion is negative autochemotaxis. A theoretical model including a concentration field around the droplet [33,35,36] can be used to elucidate the observed motions in this study. This system can be used as a physical model to understand the collective behavior of microorganisms undergoing chemotactic motion. The droplet studied in this research can also propel itself even in an isotropic phase, and the effect of sedimentation can be reduced by density matching. Therefore, this system can also be used as a model for chemically driven self-propelled objects.

ACKNOWLEDGMENTS

The authors thank Y. Maeda, Y. Iwashita, H. Hiraiwa, M. Tarama, Z. Izri, and H. Ebata for fruitful discussions. This work was supported by a JSPS KAKENHI Grant (No. JP26287100) and by an Innovative Areas “Fluctuation & Structure” (Grants No. JP25103011 and No. JP25103012) from MEXT, Japan.

[1] T. Vicsek and A. Zafeiris, Phys. Rep. **517**, 71 (2012).
[2] C. Bechinger, R. D. Leonard, H. Löwen, C. Reinchhardt, G. Volpe, and G. Volpe, Rev. Mod. Phys. **88**, 045006 (2016).
[3] E. Lauga and T. R. Powers, Rep. Prog. Phys. **72**, 096601 (2009).
[4] M. C. Marchetti, J. F. Joany, S. Ramaswamy, T. B. Liverpool, J. Prost, M. Rao, and R. A. Simha, Rev. Mod. Phys. **85**, 1143 (2013).
[5] T. Ohta, J. Phys. Soc. Jpn. **86**, 072001 (2017).

[6] C. C. Maass, C. Krüger, S. Herminghaus, and C. Bahr, Annu. Rev. Condens. Matter Phys. **7**, 171 (2016).
[7] S. Nakata, Y. Iguchi, S. Ose, M. Kuboyama, T. Ishii, and K. Yoshikawa, Langmuir **13**, 4454 (1997).
[8] S. Nakata, M. Nagayama, H. Kitahata, N. J. Suematsu, and T. Hasegawa, Phys. Chem. Chem. Phys. **17**, 10326 (2015).
[9] N. J. Suematsu, S. Nakata, A. Awazu, and H. Nishimori, Phys. Rev. E **81**, 056210 (2010).
[10] T. Toyota, N. Maru, M. M. Hanczyc, T. Ikegami, and T. Sugawara, J. Am. Chem. Soc. **131**, 5012 (2009).
[11] T. Ban, T. Yamagami, H. Nakata, and Y. Okano, Langmuir **29**, 2554 (2013).
[12] T. Ban and H. Nakata, J. Phys. Chem. B **119**, 7100 (2015).
[13] T. Banno, R. Kuroha, and T. Toyota, Langmuir **28**, 1190 (2012).
[14] T. Banno, S. Miwa, R. Kuroha, and T. Toyota, Langmuir **29**, 7689 (2013).
[15] T. Banno, S. Miwa, R. Kuroha, and T. Toyota, Langmuir **33**, 5393 (2017).
[16] Y. Sumino, N. Magome, T. Hamada, and K. Yoshikawa, Phys. Rev. Lett. **94**, 068301 (2005).
[17] Y. Sumino, H. Kitahata, K. Yoshikawa, M. Nagayama, S. M. Nomura, N. Magome, and Y. Mori, Phys. Rev. E **72**, 041603 (2005).
[18] K. Nagai, Y. Sumino, H. Kitahata, and K. Yoshikawa, Phys. Rev. E **71**, 065301 (2005).
[19] H. Kitahata, N. Yoshinaga, K. H. Nagai, and Y. Sumino, Phys. Rev. E **84**, 015101 (2011).
[20] F. Takabatake, N. Magome, M. Ichikawa, and K. Yoshikawa, J. Chem. Phys. **134**, 114704 (2011).
[21] Z. Izri, M. N. van der Linden, S. Michelin, and O. Dauchot, Phys. Rev. Lett. **113**, 248302 (2014).
[22] S. Tutupalli, R. Seeman, and S. Herminghaus, New J. Phys. **13**, 073021 (2011).
[23] S. Herminghaus, C. C. Maass, C. Kruger, S. Thutupalli, L. Goehring, and C. Bahr, Soft Matter **10**, 7008 (2014).
[24] C. Krüger, G. Klos, Ch. Bahr, and C. C. Maass, Phys. Rev. Lett. **117**, 048003 (2016).
[25] T. Yamamoto and M. Sano, Soft Matter **13**, 3328 (2017).
[26] T. Hiraiwa, K. Shitara, and T. Ohta, Soft Matter **7**, 3083 (2011).
[27] M. Tarama and T. Ohta, Prog. Theor. Exp. Phys. **2013**, 013A01 (2013).
[28] K. Peddireddy, P. Kumar, S. Thutupalli, S. Herminghaus, and C. Bahr, Langmuir **28**, 12426 (2012).
[29] P. D. Todorov, P. A. Kralchevsky, N. D. Dkonc, G. Broze, and A. Mehreteab, J. Colloid Interface Sci. **245**, 371 (2002).
[30] S. Suda and M. Ichikawa (unpublished).
[31] E. Guyon, J. P. Hulin, L. Petit, and C. D. Mitescu, *Physical Hydrodynamics* (Oxford University Press, New York, 2015).
[32] I. W. Steward, *The Static and Dynamic Continuum Theory of Liquid Crystals* (Taylor & Francis, London, 2004).
[33] C. Jin, C. Krüger, and C. C. Maass, Proc. Natl. Acad. Sci. USA **114**, 5089 (2016).
[34] T. Yamamoto and M. Sano, Phys. Rev. E **97**, 012607 (2018).
[35] K. Shitara, T. Hiraiwa, and T. Ohta, Phys. Rev. E **83**, 066208 (2011).
[36] S. Yabunaka, T. Ohta, and N. Yoshinaga, J. Chem. Phys. **136**, 074904 (2012).